International Journal of Applied Earth Observations and Geoinformation 109 (2022) 102798

Contents lists available at ScienceDirect

International Journal of Applied Earth Observations and Geoinformation

journal homepage: www.elsevier.com/locate/jag

Characterizing urban growth in Vientiane from 2000 to 2019 using time-series optical and SAR-based estimates of urban land

Chong Huang [a,*,1], Chenchen Zhang [a,b,1]

[a] State Key Lab of Resources and Environmental Information System, Institute of Geographic Sciences and Natural Resources Research, Chinese Academy of Sciences, Beijing, China
[b] University of Chinese Academy of Sciences, Beijing, China

ARTICLE INFO

Keywords:
Urban land
Time-series remote sensing
Small and medium-sized city
Urban expansion
Vientiane

ABSTRACT

While annual urban growth rates are declining in many highly urbanized regions of the world, Southeast Asia (SEA) is experiencing an accelerated urbanization process in small and medium-sized cities (SMCs), to which little attention has been paid. High-precision urban land information is a prerequisite for analyzing urban expansion characteristics for SMCs. However, accurately extracting urban land information for SMCs in SEA has remained challenging, considering the lower urban land density, higher vegetation cover, and complex landscape mosaic. This study systematically analyzed the capacities of a set of statistical indicators of time-series optical and synthetic aperture radar (SAR) images in impervious surface extraction. Then, an automatic urban land mapping method was developed by integrating time-series optical and SAR statistical indicators to map urban land area at a finer spatial resolution. The method was applied to Vientiane, Laos, as a case to explore the characteristics of the rapid urbanization process over 2000–2019 and problems related to sustainable urban development. Our results show the statistical indicators of SWIR1, SWIR2, VV, and VH can distinguish urban land from bare soil and cropland, and statistical indicators of NDVI can separate urban land from seasonal vegetated land. The overall accuracies of our products on Vientiane exceeded 95%, and the kappa coefficient was close to 0.90. The study found that the city was experiencing accelerated urban growth, and the urban land area increased from 25.93 km^2 in 2000 to 37.23 km^2 in 2010 and 62.12 km^2 in 2019. Spatially, the urbanization patterns of Vientiane showed a certain degree of sprawl, especially in the suburbs. Rapid urban sprawl poses a significant threat to the urban environment and sustainable development.

1. Introduction

Southeast Asia (SEA) has witnessed a notable increase in the urbanization process since 2000. Over the past two decades, the region has become one of the most economically active regions in the world due to the increased role of ASEAN (Association of Southeast Asian Nations) in the world economy (Schneider et al., 2015). With the acceleration of industrialization, village dwellers have moved to and settled in cities for the improvement of their livelihood. As a result, many small and medium sized cities (SMCs) have expanded rapidly (UNDESA, 2019). In contrast to rates less than 1% in many developed countries (UNDESA, 2012), the annual urban growth rate in SEA is relatively high at 2.38%. Rapid urbanization and urban land encroachment are highly likely to bring adverse ecological, economic, and social consequences (Sharifi et al., 2014). Although many studies have been implemented to explore rapid urbanization, most studies on remotely sensing urban expansion have focused on high- or middle-income countries such as the U.S. or China (Reba and Seto, 2020), or on large cities and mega-cities with more than 5 million people (Taubenböck et al., 2012), while little attention has been paid to the rapid expansion of SMCs in SEA.

Remote sensing-based impervious surface extraction is one of the key issues in urban expansion studies. Since 1980 s, many methods have been proposed to extract impermeable surfaces from multi-source remotely sensed images (Wang and Li, 2019), most of which were based on optical remote sensing images. Considering the relatively dispersed urban morphology, Landsat-like data with 30 m spatial resolution have often been used for urban analysis (Wang et al., 2019; Liu et al., 2019; Deng and Zhu, 2020). However, spectral confusions among

* Corresponding author.
E-mail addresses: huangch@lreis.ac.cn (C. Huang), zhangcc.17s@igsnrr.ac.cn (C. Zhang).
[1] These authors contributed equally to this work.

https://doi.org/10.1016/j.jag.2022.102798
Received 8 May 2021; Received in revised form 14 April 2022; Accepted 19 April 2022

different urban land covers are main problems when a single date or multiple-date imageries were used for classification. For example, bare soil is spectrally confused with bright impermeable surfaces. In addition, the acquisition of enough good-quality (not affected by clouds and cloud shadows) observations is another challenge in cloudy regions (Henderson and Xia, 1997; Leinenkugel et al., 2011). Unlike optical data, synthetic perture radar (SAR) has all-weather observation capability and is not affected by clouds, thus can reduce the errors induced by bad-quality observations in optical images (Wang and Li, 2019). Moreover, SAR can capture the structural and dielectric properties of the Earth's surface materials and are sensitive to geometric features of urban land surfaces, which can be complementary to spectral features of optical images (Lin et al., 2020). Recent years, combing SAR and optical images to improve the impervious surface estimation has become popular in remote sensing domain. Correspondingly, several global land cover datasets (including impervious surface category) and thematic urban impervious surface datasets have been generated and applied to global- or national- scale impervious surface change analysis or metropolitan expansion monitoring (Gong et al., 2020; Sexton et al., 2013). However, when applied to SMCs in SEA, the accuracy of these data is still in question. Fluctuating variations in ground objects remain a major challenge for both optical and synthetic aperture radar imaging (Wang and Li, 2019).

To tackle this problem, a few studies have used time-series data to reduce the errors in land cover classification as they can capture the phenological difference of vegetated land surface (Guan et al., 2015; Huang et al., 2020; Sun et al., 2019; Wang et al., 2019). The approaches can be grouped into two categories according to the way temporal information used: time series similarity measurement and time series statistical metrics (Lhermitte et al., 2011). In the former method, time series profile of each pixel or object was reconstructed, then compared with reference time series by using distances. The key process generally consists of comparing data in order to estimate a (dis)similarity (Petitjean et al., 2012). This method requires dense higher quality images to build a whole time series, which limited its use in cloud-prone tropical SEA. Meanwhile, in time series statistical metrics approach, the statistical features of different types of land cover evolution were calculated from time series data stack, then fed into a classifier to improve the capacity for discernment among different categories (Wang et al., 2019). Statistical metrics have less stringent requirements regarding cloud contamination in time-series remote sensing images. In addition, statistical computation is simpler and more efficient compared with other time-series analysis methods. In our previous research, statistical metrics from time series optical data were employed in land cover classification, and such metrics showed high capacity in identifying bright impervious surfaces due to the robustness in characterizing seasonal changes in the land surface (Huang et al., 2020). We supposed that incorporating of time series SAR should contribute to the urban impervious surface discriminating, especially for dark impervious surface with different material.

Although a few studies have tested time series SAR data for land cover classification at large scale, in which a simple threshold method was applied to SAR statistical indicators to generate the potential urban land mask (Sun et al., 2019; Gong et al., 2020), a fixed threshold cannot be applied to delineate the urban impervious land at a finer scale considering the diverse urban landscape and complex impervious material cover. An accurate and robust urban land mapping method that integrates time series optical and SAR data is urgently needed for supporting small and medium-sized cities studies.

To address these issues, we proposed a synergistic approach to integrating the complementary optical and SAR data under the machine learning framework using a set of robust statistical metrics, improve the accuracies of urban impervious surface for SMC urban expansion studies. The objectives of this study are: (1) to investigate the capacities of different statistical indicators of time-series optical and SAR images in urban impervious surface extraction; (2) to integrate time-series SAR and optical indicators to map urban land area for SMCs at a finer spatial resolution; and (3) to apply our method to investigate the temporal and spatial patterns of urban expansion of Vientiane over the period 2000–2019.

2. Material and methods

2.1. Study area

Vientiane, the capital of Laos, is located near the middle of the country's north–south extent, on the bank of the Mekong River (Fig. 1). It features a tropical climate with an average annual maximum and minimum temperature of 31.1℃ and 21.8℃, respectively. The annual average rainfall is 1,660.5 mm (WWIS, 2012). Since the Laos government initiated the New Economic Mechanism (NEM) in 1986, Vientiane has received substantial government and foreign direct investment to improve the transport infrastructure (Sharifi et al., 2014). As a result, Vientiane is experiencing a fast urban expansion which can be typically observed in many SMCs of SEA (UNDESA, 2012). According to the master plan of central Vientiane Capital (planned by the JICA study team, 2010), the urban area in this study is surrounded by the '450 Year Road', Route 13 North, and Rue Thadeua, with the Mekong River as its natural border to the south (Fig. 1). Despite the rapid expansion, most of the suburban area remains essentially pre-industrial, and has a high level of forest coverage, also with large areas of paddy fields and marshlands.

Vientiane has five main land cover types: urban land, bare soil, forest, cropland, and water body. In this study, urban land refers to places dominated by the 'built environment', including all impervious surfaces and human-constructed elements (e.g., roads, buildings) (Schneider et al., 2010). In optical images, urban land composed of metal or new concrete has high reflectance, making it appear bright, while urban land made up of asphalt or old concrete has low reflectance and tends to appear dark. Therefore, we further divided urban land into bright urban land and dark urban land.

2.2. Data and processing

2.2.1. Sentinel-2 and Landsat

70 Sentinel-2 images for 2019, 9 Landsat TM images, 13 Landsat ETM + images for 2010, and 18 Landsat TM images and 5 Landsat ETM + images for 2000 were collected from Google Earth Engine (GEE). Good observations were obtained by removing clouds and cirrus using the BQA (Landsat) or QA60 (Sentinel-2) bitmask band with cloud mask information. Three widely used vegetation indices including Nominalized Difference Vegetation Index (NDVI) (Tucker, 1979), Enhanced Vegetation Index (EVI) (Huete et al., 2002; Huete et al., 1997), Land Surface Water Index (LSWI) (Xiao et al., 2004; Xiao et al., 2005) were calculated for each imagery using Eqs. (1)–(3):

$$NDVI = \frac{\rho_{NIR} - \rho_{Red}}{\rho_{NIR} + \rho_{Red}} \tag{1}$$

$$EVI = 2.5 \times \frac{\rho_{NIR} - \rho_{Red}}{\rho_{NIR} + 6 \times \rho_{Red} - 7.5 \times \rho_{Blue} + 1} \tag{2}$$

$$LSWI = \frac{\rho_{NIR} - \rho_{SWIR1}}{\rho_{NIR} + \rho_{SWIR1}} \tag{3}$$

where ρ_{Blue}, ρ_{Red}, ρ_{NIR}, and ρ_{SWIR1} are the surface reflectance values of Blue, Red, NIR, and SWIR1 bands for Landsat and Sentinel-2 images.

2.2.2. Sentinel-1 and ALOS PALSAR-2

122 Setninel-1 images for 2019 were collected from GEE. Sentinl-1 data have dual-polarization of vertical transmitting with vertical receiving (VV) and vertical transmitting with horizontal receiving (VH) bands (Torres et al., 2012). Sentinel-1 data in GEE was pre-processed with the Sentinel-1 Toolbox using the orbit metadata update, GRD

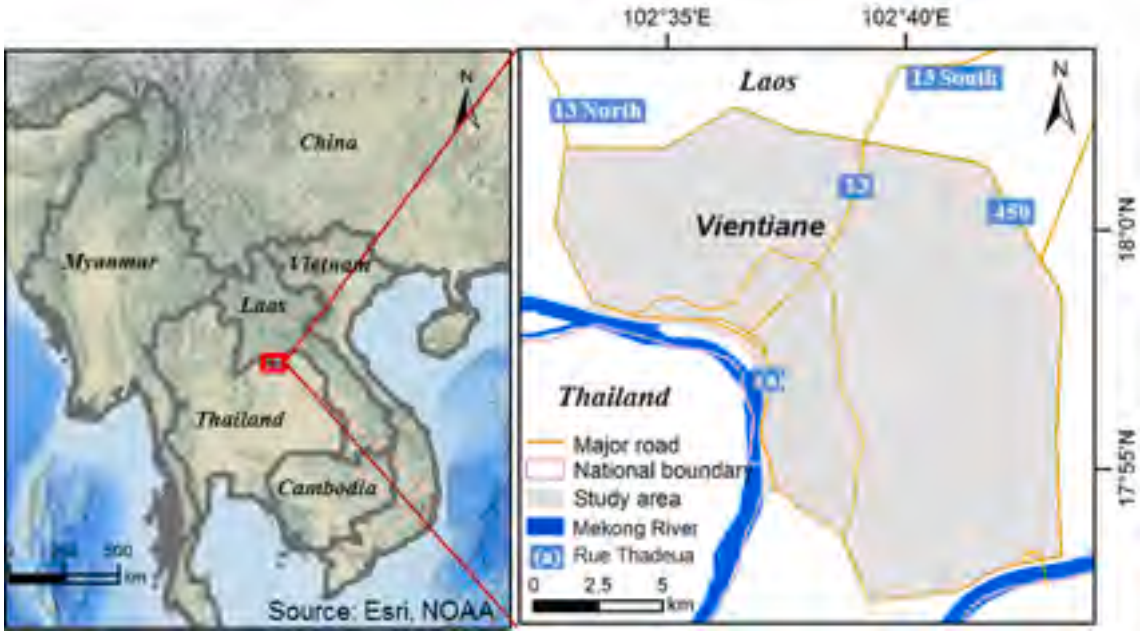

Fig. 1. Location of the study area.

border noise removal, thermal noise removal, radiometric calibration, and terrain correction. A Refined Lee filter was applied to de-speckle the images. The final terrain-corrected values were converted to decibels (dB) in each pixel via log scaling $10\log_{10}(DN)$.

The ALOS PALSAR-2 mosaic imagery in 2010 were used in the urban land identification in 2010. PALSAR-2 imagery in GEE was *ortho*-rectified and slope corrected using the 90 m SRTM Digital Elevation Model. For each year and location, the strip data were selected through visual inspection of the mosaics available over the period, with those showing minimal response to surface moisture preferentially used. The DN values in PALSAR HH and HV bands were converted to gamma naught values in decibel units (dB) using $\gamma_0 = 10\log_{10}(DN^2) - 83.0$ (Shimada et al., 2009). The 25 m PALSAR imagery was resampled into 30 m imagery to match the spatial resolution of Landsat imagery using nearest neighbor interpolation.

2.2.3. Reference data for cross validation

We collected three other urban land products to compare the consistency and differences with our urban land result in 2019: (1) 10 m Finer Resolution Observation and Monitoring of Global Land Cover (FROM-GLC10) for 2017 (Gong et al., 2019). We used the impervious surface layer labeled as 80 in FROM-GLC10 to compare our results; (2) 20 m Global Human Settlements Layer using Sentinel-1 (GHS-S1) data for 2016 (Corbane et al., 2018); and (3) an annual global urban dynamics product, the 30 m Global Artificial Impervious Area (GAIA) between 1985 and 2018 (Gong et al., 2020). Annual impervious area maps were merged to obtain the urban land layer in 2018.

2.2.4. Ground reference for training and accuracy assessment

1,000 sample points were randomly generated and manually interpreted for approach training. For each point, historical very high resolution (VHR) Google Earth images, and available Landsat and Sentinel-2 imagery in 2000, 2010, and 2019 were used to interpret the land use type. The points without clear land cover information due to unavailable reference or cloud interference were excluded. Points with inconsistent land use types in the three years will also be excluded. The points that maintain the same land use type in all 3 years will be selected. In total, 70 bright urban land points, 86 dark urban land points, 64 bare soil points, 72 forest points, and 64 cropland points were used as stable training data over the three target years.

Another 1000 sample points were prepared for accuracy assessment of the resultant urban land and non-urban land map for each year. In total, urban land had 230, 283, and 342 validation points, and non-urban land had 770, 717, and 658 validation points for years 2000, 2010, and 2019, respectively. Additionally, to compare the accuracy of our urban land results with other urban land products, we also labeled these 1000 validation points for 2016, 2017, and 2018.

2.3. Urban land extraction framework

We proposed an automatic urban land mapping framework by integrating time-series optical and SAR imagery to extract urban land areas in Vientiane, Laos, in 2010 and 2019. In order to explore the process of urban expansion, we also extracted urban land areas for 2000 using time-series optical data only, due to the lack of available SAR data. The spatial resolution of the urban land results is 10 m for 2019 and 30 m for 2000 and 2010, depending on the spatial resolution of the available satellite images. The overall framework for the urban land extraction in 2019 is shown in Fig. 2. The urban land extraction process for 2010 and 2000 is similar to that of 2019.

2.3.1. Water area masking

Before extracting the urban land, we first excluded water bodies in each year, as water has similar backscattering characteristics with some impervious surfaces in SAR imagery (Zou et al., 2018) and has similar spectral reflectance with dark impervious surfaces in optical imagery (Lu and Weng, 2006). Pixels with a water frequency (WF) value $\geq 80\%$ were identified as a year-long water body (Qin et al., 2017). WF per pixel was calculated based on the criteria in Eq. (4) (Xiao et al., 2006):

$$\mathrm{WF} = \frac{N_{LSWI-EVI\geq 0}}{N_{Gqos}} \tag{4}$$

where $N_{LSWI-EVI\geq 0}$ is the number of observations with $LSWI - EVI \geq 0$ from high-quality observations; N_{Gqos} is the number of good-quality observations; and WF is the ratio of observations with $LSWI - EVI \geq 0$ out of all good observations in 1 year.

2.3.2. Deriving temporal statistical indicators

Time-series NDVI statistical indicators have been proved useful for land cover extraction (Qin et al., 2017; Sun et al., 2019). SWIR bands are

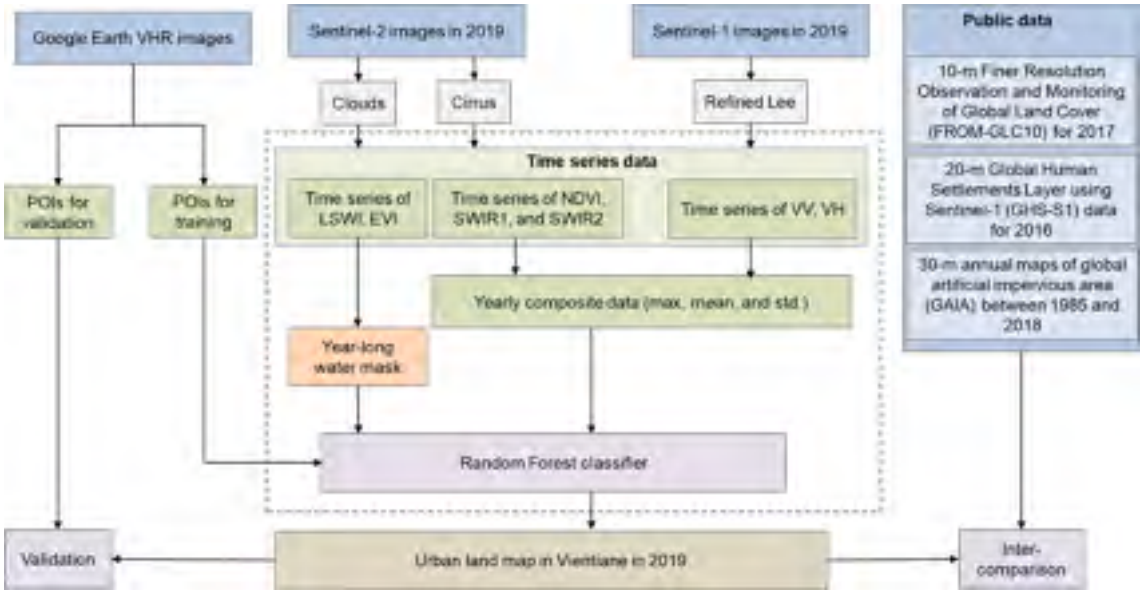

Fig. 2. Workflow for mapping urban land in Vientiane in 2019.

also suited for distinguishing different types of impervious surfaces (Herold et al., 2003). In our study, we calculated the mean and standard deviation values of NDVI, SWIR1 and SWIR2 (i.e., NDVI_max, NDVI_mean, NDVI_std, SWIR1_mean, SWIR1_std, SWIR2_mean, SWIR2_std) from annual time-series optical images in 2019, 2010, and 2000. We also calculated the maximum value of NDVI (i.e., NDVI_max). Similarly, the mean and standard deviation values of VV and VH (i.e., VV_mean, VH_mean, VV_std, and VH_std) were also calculated from annual time-series Sentinel-1 SAR images in 2019. All these statistical indicators were further used as classification features to differentiate urban impervious surfaces from other land cover types. The features for urban land classification in 2000, 2010, and 2019 are shown in Table 1.

2.3.3. Urban land extraction

Random Forest (RF) classifier (Belgiu and Drăguţ, 2016) was selected to generate an urban land map using the statistical indicators (Table 1) of the specific year. RF classifier has high efficiency and high accuracy in processing high-dimensional, massive data compared with other machine learning algorithms (Belgiu and Drăguţ, 2016). Considering the difference in data sources used for each year, different features were incorporated to construct the RF model for urban land classification in 2000, 2010, and 2019 (Table 1). The number of decision trees (numberOfTrees, the number of trees created by randomly selecting samples from training samples) was set to 100. The other parameters were set by default in GEE in order to avoid overfitting, as recommended by Liaw and Wiener (2002).

Table 1
Features used for urban land extraction.

Year	Optical statistical indicators	Features of SAR imagery
2000	NDVI_max, NDVI_mean, NDVI_std, SWIR1_mean, SWIR1_std, SWIR2_mean, SWIR2_std derived from Landsat time series	SAR data unavailable
2010	NDVI_max, NDVI_mean, NDVI_std, SWIR1_mean, SWIR1_std, SWIR2_mean, SWIR2_std derived from Landsat time series	HH, HV of PALSAR-2
2019	NDVI_max, NDVI_mean, NDVI_std, SWIR1_mean, SWIR1_std, SWIR2_mean, SWIR2_std derived from Sentinel-2 time series	VV_mean, VV_std, VH_mean, and VH_std derieved from Sentinel-1 time series

2.3.4. Accuracy assessment of the urban land maps

The urban land classification results in 2019, 2010, and 2000 were validated using confusion matrices (Foody, 2002). Indicators including overall accuracy (OA), kappa coefficient, producer's accuracy (PA), and user's accuracy (UA) were used to quantitatively assess the accuracy of urban land maps. Moreover, the three other urban land products (i.e., FROM-GLC, GHS-S1, and GAIA) were also evaluated in comparison with our results.

2.4. Urban growth analysis

2.4.1. Urban expansion dynamics

Two indicators including urban expansion rate (ER) (Eq. (5)) and annual growth rate (AGR) (Eq. (6)) were used to evaluate the temporal rate of urban expansion (Zhao et al., 2018).

$$ER = \frac{S_{T2} - S_{T1}}{S_{T1}} \times \frac{1}{N} \times 100\% \tag{5}$$

$$AGR = \left[\left(\frac{S_{T2}}{S_{T1}} \right)^{\frac{1}{N}} - 1 \right] \times 100\% \tag{6}$$

where S_{T2} and S_{T1} are the urban land area at times T_2 and T_1, respectively, and N is the interval between two periods (in years).

An urban land density distance function f (Eq. (7)) proposed by Jiao (Jiao, 2015) was used to fit the decay of the urban land density to the distance to the city center:

$$f(r) = \frac{1 - c}{1 + e^{\alpha((2r/D)-1)}} + c \tag{7}$$

where f is urban land density, r is the distance from a concentric ring to the urban center, e is Euler's number, and α, c, and D are parameters. The parameter c represents the background value of urban land density in the hinterland of a city, D indicates the approximate extent of a city, and α is used to measure the compactness of the city, where a higher value indicates a more compact urban form. Parameters c and D will increase as the urban area expands (Jiao, 2015).

Concentric ring division is widely used to analyze urban land density variation, which ensures equal measurement of urban growth in any direction to identify the possible trend in certain positions (Jiao, 2015; Xu et al., 2019a). We calculated urban land density based on concentric ring partitioning, i.e., the ratio of urban land area to the buildable area

in each ring. We took the birthplace of Vientiane (around the government quarter) as the city center by inspecting historical VHR images in Google Earth. Considering the extent of Vientiane city, we tested the effect of different radius values of concentric ring (namely 0.5 km, 1 km, and 1.5 km) on urban expansion. Although they had a subtle effect on the calculation results, the overall trends were similar. We finally selected 0.5 km as the buffer distance. Then, a series of equidistant (0.5 km) concentric rings were created from the city center to the outermost ring that almost covers the entire urban land. The non-linear least squares method was employed to fit the urban land density distance function with Matlab 2017a (Martinez et al., 2017).

2.4.2. Urban expansion patterns

Urban expansion is generally divided into infilling, edge-expansion, and leapfrogging (Fei and Zhao, 2019). Infilling refers to the formation of new urban patches by filling gaps within existing urban patches. Edge-expansion is defined as a new urban patch extending outward along the edge of existing urban patches. If the expanded patch does not overlap with any existing urban patches, then it is considered leapfrogging. These three types of urban expansion were identified using the metric E (Eq. (8)) (Fei and Zhao, 2019):

$$E = \frac{L_{com}}{P_{new}} \tag{8}$$

where L_{com} is the length of the common border between the new urban patch and existing urban patches, and P_{new} is the perimeter of the new urban patch. Leapfrogging occurs when $E = 0$, edge-expansion when $0 < E \leq 0.5$, and infilling when $0.5 < E \leq 1$.

3. Results

3.1. Capacities of different statistical indicators in differentiating impervious surface from other land cover

Fig. 3 shows the two-dimensional scatter plot/density maps of the representative urban land pixels along with three other types of non-urban land pixels (i.e., forest, cropland, and bare soil) collected from Vientiane in 2019. Different land cover types hold their specific distribution patterns in SWIR, NDVI, VV and VH statistical indicators. The SWIR_mean values for urban land and bare soil are around 0.2–0.4 and greater than 0.4, respectively. The average SWIR_std values for urban land and bare soil are around 0.05–0.075 and 0.1, respectively. Therefore, SWIR is helpful to distinguish between urban land and bare soil, as bare soil is larger than urban land in both the mean and standard deviation of SWIR annual time series (Fig. 3a, b). NDVI_max can effectively distinguish urban land from forest and cropland, as urban land has a relatively low amount of vegetation throughout the year, and its NDVI_max values are around 0.2, while forest and cropland have large vegetation during the peak growing season and their NDVI_max values are around 0.9 and 0.7, respectively. The NDVI_mean and NDVI_std can reflect the phenological characteristics and inter-annual varieties of vegetation (e.g., forest, cropland). The NDVI_mean values in cropland (around 0.3) and forest (around 0.7) are significantly greater than in urban land (around 0) (Fig. 3c). NDVI_mean values for bare soil (around 0.1) are also greater than those for urban land. Furthermore, cropland and forest exhibited a larger NDVI_std value than urban land, indicating NDVI on urban land remains relatively stable at smaller values throughout the year (Fig. 3d).

SAR imagery doesn't have an apparent difference in dark urban land and bright urban land, so the values of VV and VH statistical indicators of dark urban land and bright urban land samples are very similar (Fig. 3e, f). Urban land and other land cover types differ significantly in VV and VH statistical indicators values. For example, both dark and bright urban land have higher values in VV_mean and VH_mean due to their strong corner reflectance, which is significantly higher than bare soil and cropland. Forest likewise has higher VV_mean and VH_mean values due to its complex structure and internal reflective conditions, but is still weaker than those of urban land (Fig. 3e, f). The roughness of urban land, bare soil and forest varied slightly throughout the year, so the variation in backscatter values is small, resulting in small standard

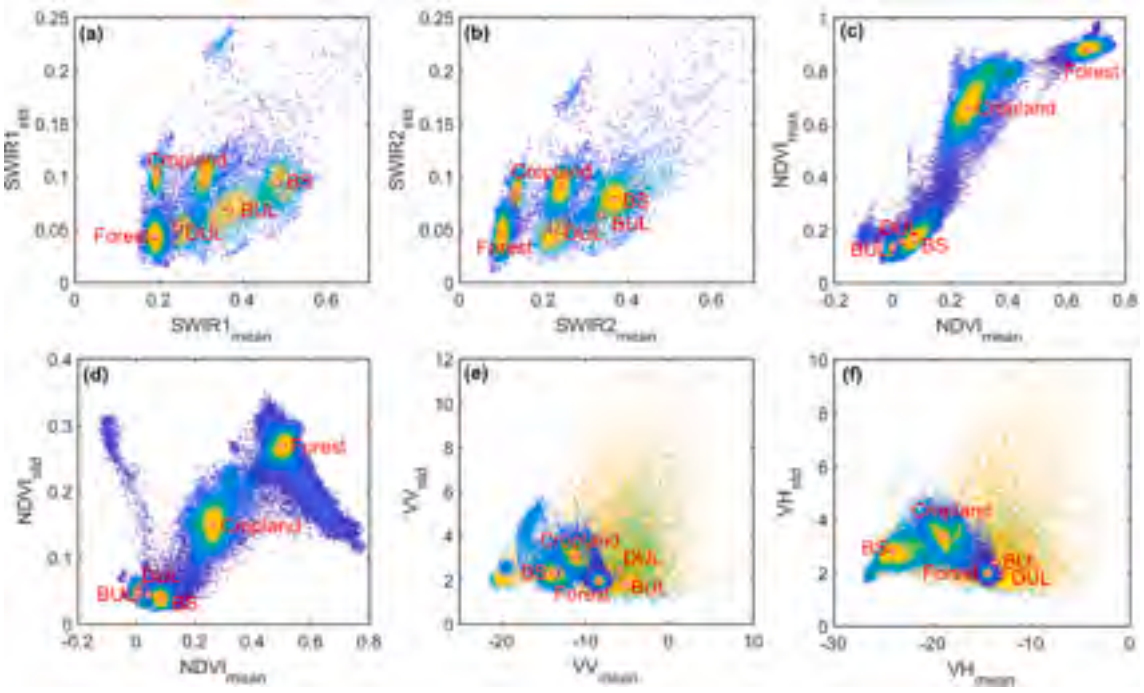

Fig. 3. Two-dimensional scatter plots of (a) SWIR1_mean and SWIR1_std, (b) SWIR2_mean and SWIR2_std, (c) NDVI_mean and NDVI_max, (d) NDVI_mean and NDVI_std, (e) VV_mean and VV_std, and (f) VH_mean and VH_std of Vientiane in 2019. The red crosses are the core values of typical land cover type distributions. (BS: Bare soil; BUL: Bright urban land; DUL: Dark urban land). (For interpretation of the references to colour in this figure legend, the reader is referred to the web version of this article.)

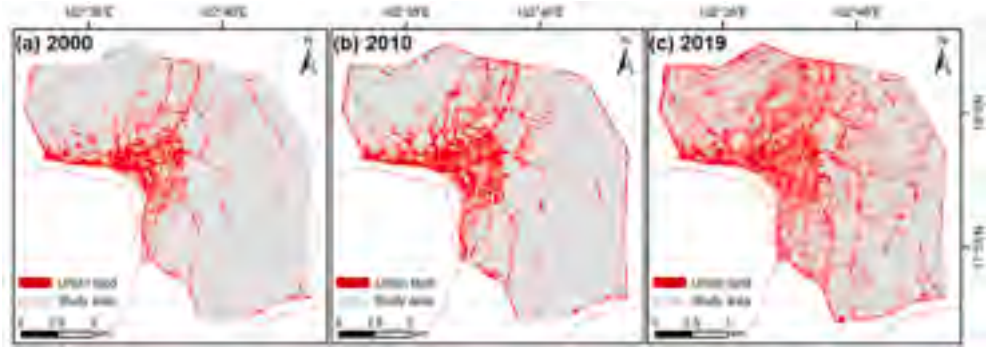

Fig. 4. Urban land maps in 2000, 2010, and 2019.

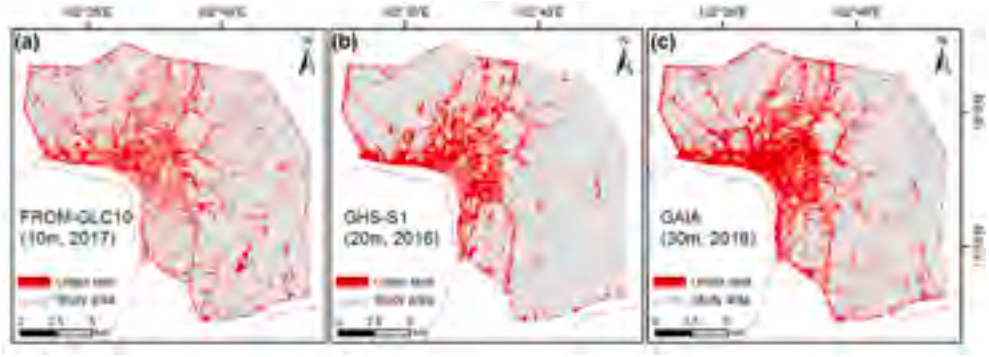

Fig. 5. Urban land maps of Vientiane by (a) FROM-GLC10 in 2017, (b) GHS-S1 in 2016, and (c) GAIA in 2018.

deviations of VV and VH for these types. Bare soil has slightly larger standard deviation of VH than urban land and forest, as VH is more sensitive to changes in soil moisture. The standard deviation of VV and VH for cropland is greater than for urban land, forest, and bare soil because the roughness varies greatly during the year due to sowing, growing, and harvesting. Therefore, the mean values of VV and VH are useful to distinguish urban land from cropland and bare soil, and the standard deviation of VV and VH are useful to identify urban land from cropland.

In summary, statistical indicators of SWIR1, SWIR2, VV, and VH can distinguish urban land from bare soil and cropland, and statistical indicators of NDVI can separate urban land from vegetation (cropland and forest). The optical and SAR statistical indicators can be integrated to assist in a more accurate urban land classification.

3.2. Urban land extraction and accuracy assessment

The urban land maps derived in 2000, 2010, and 2019 are shown in Fig. 4. We calculated the confusion matrix based on the urban land and non-urban land validation points for each year. The overall accuracies of the three urban land maps exceeded 95%, considered good results for remote sensing image-based analysis. The kappa coefficient of all results was close to 0.90. The PAs were 89.13%, 92.93%, and 95.03%, and the UAs were 90.31%, 92.61%, and 95.59% for 2000, 2010, and 2019, respectively.

We also verified and compared the accuracy of our optical/SAR-based urban land map in 2019 with other urban land products, using the validation points in the same period as each product. Fig. 5 showed the spatial distributions of the urban land maps from FROM-GLC10 (2017), GHS-S1 (2016), and GAIA (2018). Generally, our urban land map in 2019 and the three public urban land products showed a similar spatial pattern. Our results had the highest overall classification accuracy of 96.80% among the four urban land products (Fig. 6). In particular, the PA of our results reached 95.03%, while the PA values of

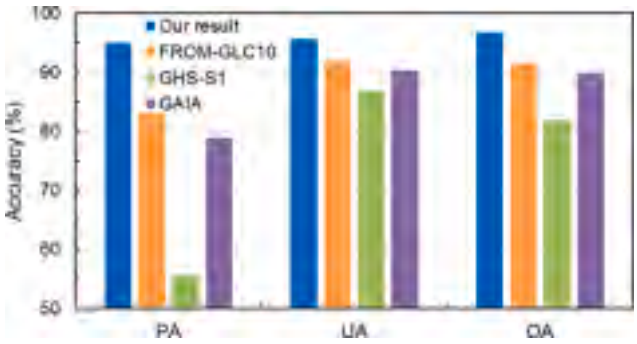

Fig. 6. Accuracy assessment (PA, UA, and OA) of our result in 2019 and other public data.

FROM-GLC10 and GAIA were around 80% but only 55.56% for GHS-S1 (Fig. 6), which indicates the omission error is relatively high in the existing public products, resulting in underestimation of urban land area, especially for GHS-S1.

3.3. Dynamics of Vientiane urbanization

Table 2 shows that the urban area of Vientiane increased from 25.93 km^2 in 2000 to 37.23 km^2 in 2010, and 62.12 km^2 in 2019. The ER and AGR values between 2010 and 2019 were 7.43% and 5.79%, respectively, which were larger than those between 2000 and 2010, indicating the urban land area in the second decade experienced more rapid growth.

Fig. 7 shows the spatial distribution of urban land in 2000, 2010, and 2019. Generally, Vientiane was characterized by continuous urban expansion from 2000 to 2019. Urban area became denser between 2000 and 2019, and the territory encroached into the forests and paddy fields in the suburbs, especially after 2010. Additionally, there was an obvious increase in the number and area of urban land along major

Table 2
Urban areas in 2000, 2010, and 2019; and expansion rate and annual growth rate in two time periods (2000–2010, 2010–2019).

Year	Urban land area (km^2)	Time period	ER (%)	AGR (%)
2000	25.93			
2010	37.23	2000–2010	4.36	3.68
2019	62.12	2010–2019	7.43	5.79

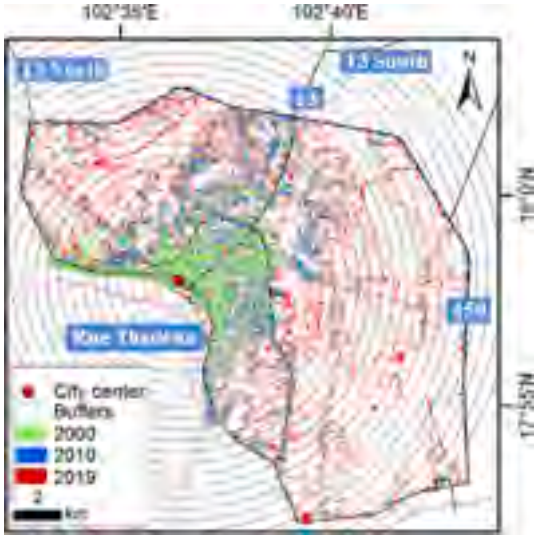

Fig. 7. Spatial distribution of the urban extent of Vientiane in 2000, 2010, and 2019, and a series of concentric rings with a 0.5 km interval.

transportation corridors like national roads.

Scatter plots and fitted curves of urban land density are shown in Fig. 8, and the estimated parameters for urban land density functions are shown in Table 3. Spatially, urban land densities in concentric rings decrease from the city center to the fringe, dropping down quickly and then decreasing slowly (Fig. 8). The urban land density in each concentric ring increased in the period 2000–2010 and further in 2019. Obviously, urban land densities in 2010–2019 were larger than those in 2000–2010, which is consistent with the trend of ER and AGR (Table 2). Parameter α increased in the first period (2000–2010) and then declined in the second period (2010–2019), meaning the spatial relationship between the new urban patches and the existing urban patches shifted from compact to dispersed. The urban extent increased in 2000–2019, as

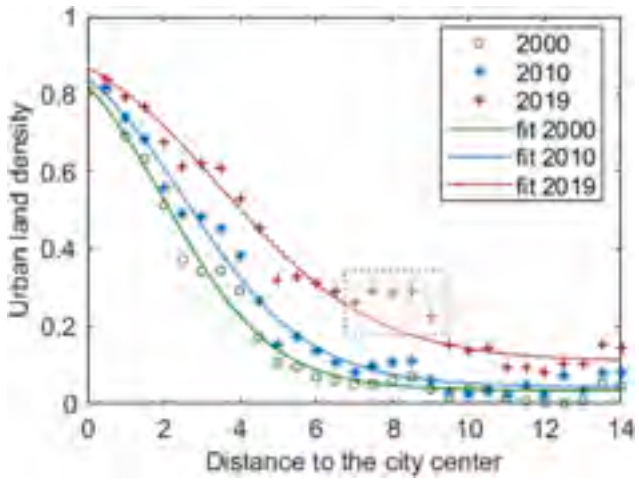

Fig. 8. The fitted urban land density functions in 2000, 2010, and 2019.

Table 3
Parameters of the fitted urban land density functions in 2000, 2010, and 2019.

	α	c	D	SSE	R^2
2000	1.52	0.03	4.23	0.02	0.98
2010	1.62	0.04	5.20	0.03	0.98
2019	1.56	0.11	7.08	0.05	0.97

the parameters c and D increased with time. In addition, there was an obvious bump in the urban land density from 7 km to 9 km in 2019 (box in Fig. 8), thus indicating a possible sub-center.

3.4. Patterns of Vientiane's urban expansion

Fig. 9 demonstrated the spatial distributions of the urban expansion patterns from 2000 to 2019 for Vientiane. Generally, urban expansion was dominated by leapfrogging and edge-expansion growth, which are the most typical characteristics of a fast urbanization process.

Leapfrogging mostly happened in the area within the early stage of urbanization, characterized by scattered or isolated urban land patches in small areas. In the first period, leapfrogging patches were mainly distributed in the northeastern part of Vientiane, with an area of 3.60 km^2. From 2010 to 2019, the area of the leapfrogging increased to 7.15 km^2, nearly a two-fold increase. A significant increase in leapfrogging has occurred in the southeast, a formerly untapped area.

Following the leapfrogging patches, edge-expansion has been the main form of urban development of Vientiane. Between 2000 and 2010, edge-expansion growth was mainly present in the northeast to the core area, with an area of 5.18 km^2, while between 2010 and 2019, the area of edge-expansion increased to 14.77 km^2, which is almost three times that of the first period. Also, edge-expansion patches can be found throughout the suburbs in the second phase.

Infilling patches often denote a later stage of the urbanization process, through filling gaps within existing urban patches. In both periods, most infilling patches happened in the core area, with areas of 2.52 km^2 and 2.98 km^2, respectively, indicating that Vientiane has not yet developed a fully compact urban core area. After 2010, a certain degree of increase in infilling patches was witnessed in the northeast, indicating an obvious urbanization process along this direction.

Roadside development is another feature of Vientiane's urban expansion. Fig. 10 further clarifies the directions of the new urban patch expansion. The new development areas are primarily concentrated in the national roads including the northern (Route 13 North) (Fig. 10A), western (Route 13) (Fig. 10B), and southern (Rue Thadeua) (Fig. 10C) transportation corridors during the past two decades. The national highway '450 Year Road', which is far from the city center, was completed in 2010. Since then, urban land development along '450 Year Road' has begun to increase (Fig. 9b), resulting in an arc of development around the city center. Increased roadside development has made the boundary between the urban core and the swathes of urban areas outside the core indistinct. The new road construction that started in 2016, northwest of central Vientiane (Fig. 10E), may lead to a new urbanization hot spot.

4. Discussion

4.1. Potential of integrating time-series optical and SAR data for SMCs land estimation

Small and medium-sized cities have spatio-temporally heterogeneous landscapes with similar spectral reflectance characteristics than large cities with high-density, contiguous impervious surfaces, presenting a greater challenge for remote sensing extraction of impervious surfaces. This study built a set of statistical indicators based on time-series remote sensing images and demonstrated the ability and robustness of these metrics in identifying impervious surfaces in small and

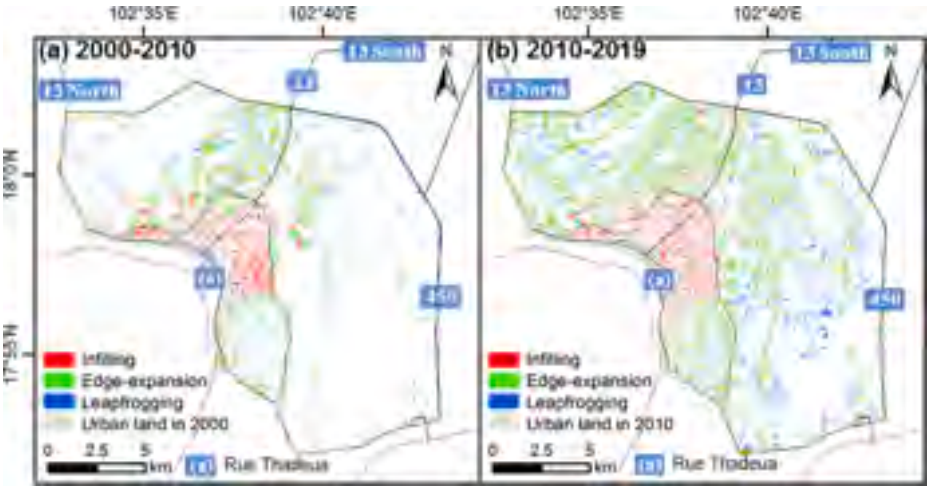

Fig. 9. Spatial distributions of the three types of urban expansion in the two periods (2000–2010 and 2010–2019) in Vientiane.

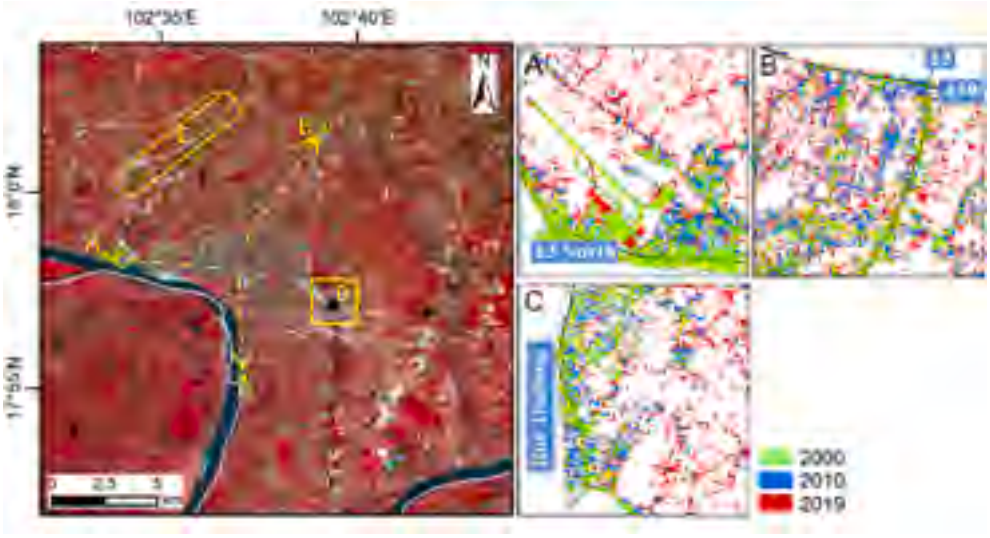

Fig. 10. Growth of urban land along the national roads.

medium-sized cities.

Time-series analysis can fully utilize all available clear pixels of the optical image stacks, which is critical for remote sensing of land cover, especially in low-latitude regions with severe cloud cover (Huang et al., 2020). Statistical indicators have a loose requirement for data acquisition time and cloud cover, which largely extends their applicability. For example, Zhang et al. (2016) showed that the SWIR band of optical images in summer can better distinguish impermeable surfaces from bare soil. However, in the middle and low latitudes, the cloud cover is severe in summer and high-quality images are difficult to obtain. Using annual time-series statistical analysis, we found in this study the annual statistical features of SWIR showed capacity to accurately distinguish impermeable surfaces from seasonal bare soil. Moreover, the method can extract the temporal variation of different land cover types (Li et al., 2018), and magnify the spectral differences between urban land and other cover. In our results, the misclassification between bright urban land and fallow cropland was greatly improved, since bright urban land had much lower mean and standard deviation of annual NDVI than fallow land once covered by seasonal crops in a yearly cycle.

One typical biophysical feature of urban land compared to non-urban land is that it is covered by various artificial impermeable materials. For spectral classification using one or several-scene images, urban land may be misclassified into different land cover types depending on the artificial impermeable materials and seasonal land surface variation. In this study, when SAR data were also incorporated for urban land extraction, we extended the feature space from the spectral to both spectral and structural dimensions to further minimize confusion. Fig. 11 shows the spatial comparison between our results (2019) and the three other urban land maps in urban core, suburb, and fringe areas. As we can see, the four products presented good consistency in the core area, although GAIA overestimated the area of urban land due to its coarse spatial resolution (30 m) and mixed pixel effect (Fig. 11a). However, all three other products underestimated urban land area in the suburbs (Fig. 11b). This low-accuracy problem in low-density urban land regions has been widely reported in many studies (Chen et al., 2015; Liu et al., 2018). Among the heterogeneous landscape, bare soil is regarded as the main disturbance in urban land detection (Zhang et al., 2016) because of its similar high reflection information and temporal statistical values are prone to be mixed up with urban land. It can be seen that a patch of bare soil in a suburban area (Fig. 11 c1, 2) was classified as urban land by both FROM-GLC10 (Fig. 11 c4) and GAIA (Fig. 11 c6), but was effectively excluded from the urban land category in our results from 2019 with the contribution of both optical and SAR statistical information (Fig. 11 c3).

In summary, our results showed a more accurate and comprehensive extraction of urban land than other products. Due to the robustness in

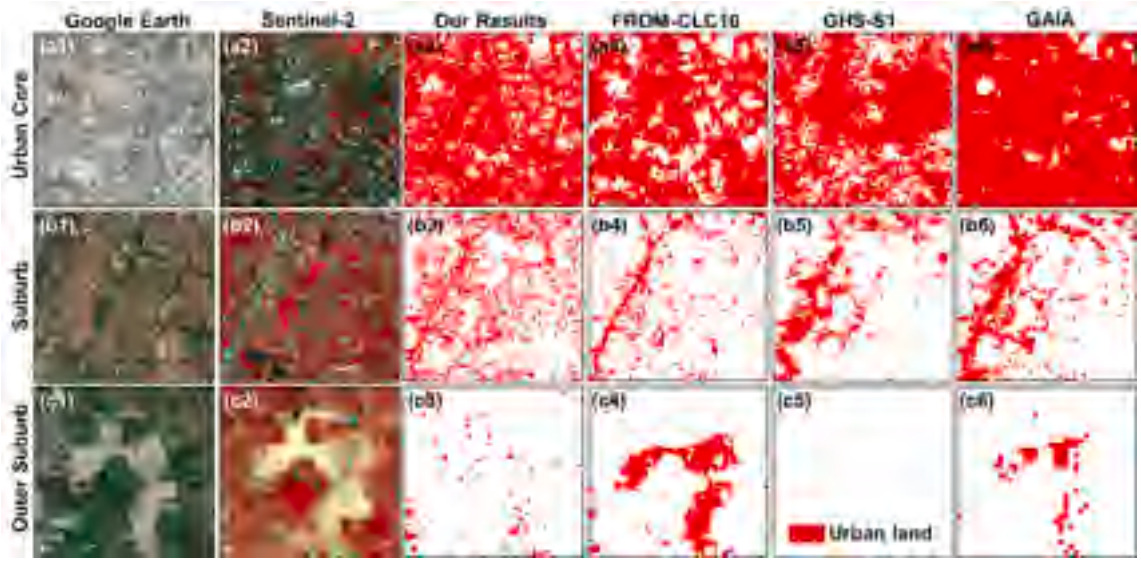

Fig. 11. Comparison of urban land maps using the Sentinel-1/2 statistical indices approach (our results), FROM-GLC10, GHS-S1, and GAIA of an (a) urban core, (b) suburb, and (c-d) outer suburb in Vientiane.

catching land surface reflectance variation both in temporal and spatial dimensions, our method is capable of more accurately identifying urban land in heterogeneous urban landscapes, and has great potential to be applied to urban expansion analysis for other SMCs.

4.2. Dynamics of urban expansion in Vientiane

The difference in AGR indicators between the two periods and the distance decay of the urban land density confirm that Vientiane is still in the primary stages of urban development. The AGR value of the second period was significantly greater than that of the first period (Table 2), while in most other developed megacities such as Melbourne, Australia (Rahnama et al., 2020), or Shanghai, China (Zhang et al., 2020), the AGR value showed an obvious decrease.

The pattern of distance decay of the urban land density is another indicator of urban development dynamics. Distance decay curves of the urban land density vary among different sizes of cities, which reveals the disparities of urban expansion and urban form among them (Xu et al., 2019a). According to the stage of city development, there are three patterns of distance decay of the urban land density, namely, the inverse S-shape, two stages of linear decay, and linear decay (Xu et al., 2019a). Urban land density of most large cities have an obvious inverse S-shape, such as those in China (e.g., Beijing, Shanghai, and Shenzhen), in Africa (e.g., Kinshasa, Luanda, and Khartoum) (Xu et al., 2019a), and in Southeast Asia (e.g., Bangkok, Manila, and Ho Chi Minh City) (Xu et al., 2019b). Our results found the pattern of distance decay in Vientiane is between the inverse S-shape and the two stages of linear decay (Fig. 8). This is partly attributed to its relatively low urban land densities. Urban land densities near the city center in Vientiane are around 80%, compared to most other large cities that are more than 90% (Xu et al., 2019a). This implies that Vientiane has not yet formed a compact urban core and therefore is far from the well-established inverse S-shape. Vientiane's urban form is still relatively dispersed compared to medium and large cities (e.g., Manila in Philippines (Xu et al., 2019b), Beijing in China (Jiao, 2015) as these cities have higher α values (usually greater than 3), whereas the α values of Vientiane are all around 1.5 (Table 3). The relatively dispersed urban form in small cities needs to be given attention, and controlling measures should be implemented in future urban planning (Xu et al., 2019a).

4.3. Spatiotemporal patterns and driving forces of urban development in Vientiane

According to population, economic conditions, and cultural factors, urban expansion can be divided into outward ring expansion (Jiao, 2015), inner-city expansion (Kuang et al., 2014), and sprawl (Cobbinah et al., 2015). Our results show that the urbanization patterns of Vientiane showed a certain degree of sprawl, especially in the suburbs. During the period 2000–2019, the pace of outward-oriented growth in Vientiane is rapid and mostly unplanned, featuring sparse, disordered, and low-density growth of *peri*-urban areas, which was also observed by Cao et al. (Cao et al., 2019) in the study of the urbanization process from 1990 to 2015.

Uncontrolled urban spatial sprawl has also been found in African cities, characterized by noncontiguous or leapfrogging growth often with low-density physical development (Cobbinah et al., 2015). The rapid increase in population is the main driving force for urban sprawl in developing countries. Rural–urban migration is the most important contributor to the increased population density in Vientiane. As the capital city and the primary economic center (Cohen, 2006), Vientiane has attracted many rural people for a better life, economic opportunities, and social services. Unlike immigrants in Africa or other Asian cities who have low income and thus have to live in the high-density central areas of the city, the preference for living in low-rise houses might also be one of the main reasons for the continued growth of urban sprawl in Vientiane, considering the relatively low living cost in suburban areas (Vongpraseuth and Choi, 2015).

As many rural people pour into cities, it is common for governments to implement orderly development strategies in cities through the process of urban growth planning. For some modern metropolitan areas in America and Europe, the originally designed master plan is integrated and the urban development often follows in step. In China, the urban expansion of many large cities, such as Beijing, Shanghai, and Guangzhou, has been strictly manipulated by master planning with less sprawl (Kuang et al., 2014). However, for Vientiane, master plans guiding urban development have rarely been successful (Cohen, 2006).

The urbanization process enormously expanded urban areas of Vientiane over the past 20 years. Transportation, unsurprisingly, played an important role in this process. As the "skeleton" of the city, the transportation network essentially directs urban development. Roadside expansion characterized urban sprawl in most cities in Southeast Asia, such as Chiang Mai and Nakhon Ratchasima, Thailand (Jongkroy and

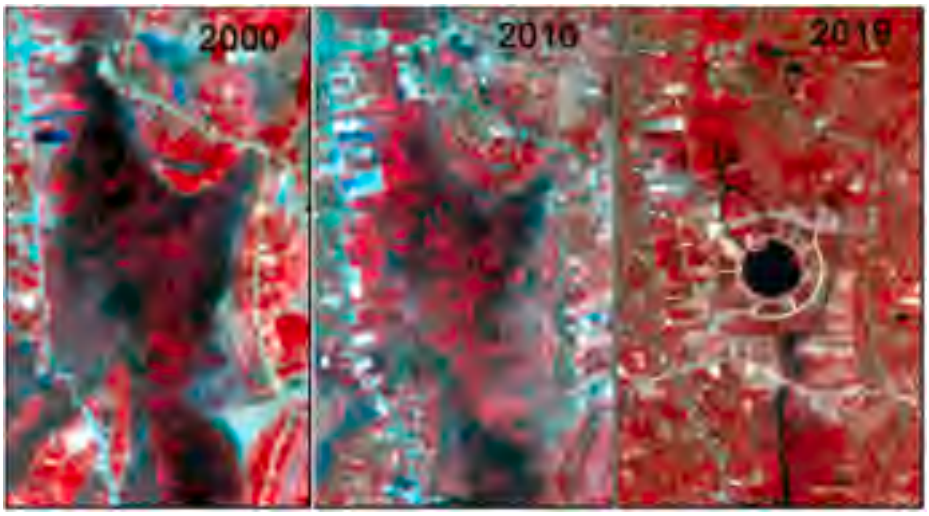

Fig. 12. Land cover change in and around the That Luang Marsh.

Thongbai, 2014), Yangon, Myanmar (Cao et al., 2019), and Hanoi, Vietnam (Mauro, 2020). Different from megacities with efficient public transport systems and higher utilization density (Kuang et al., 2014), small to medium-sized cities usually have underdeveloped transportation networks and a lower level of public transportation availability. As a result, almost all urban sprawl at the early stage happens along a few main roads. Vientiane has been growing radially during the past two decades along main roads to the south, north, and west (Figs. 9, 10). Among those, major roads contributed most to the rapid urban area expansion over the past two decades. At this rate of growth, the urban area near the intersection of the '450 Year Road' and Route 13 may become the sub-center of Vientiane (point B in Fig. 10). This kind of development alters the traditional monocentric urban form. Meanwhile, the hierarchy of trunk roads (with respect to functionality), to a large extent, determines the intensity and extent of urban growth in the region. The '450 Year Road' has encouraged urban expansion in a circular pattern around the city core and has resulted in greater urban spread at the edge of the city.

4.4. Sustainable development challenges in the urbanization process of SMCs in SEA

The worldwide urbanization process has brought positive impacts such as economic growth and improved human welfare. During the past few decades, Laos has witnessed major shifts from predominantly subsistence agrarian economies to an increasingly commercialized agricultural society (Hall et al., 2011), with a boom in the urban population and rapid urban expansion. However, during the urbanization process in Vientiane and other SMCs in SEA countries, economic development was often given more attention by the government when making decisions. Rapid urban expansion with a loose control strategy inevitably damages urban ecosystem services (Wang et al., 2018) and increases land management challenges (Niroula and Thapa, 2005). Studies have shown that uncontrolled urban expansion has led to unsustainable land development, often in the form of encroachment on surrounding rural areas and conversion of non-urban land, especially agricultural land, forests, and wetlands, to urban land use (Amoateng et al., 2013). In addition, urban sprawl often occurs in a leapfrogging manner, with adverse impacts far beyond urban boundaries (Cobbinah et al., 2015), posing a range of development threats both to socio-economic and environmental benefits.

Many SMCs in tropical SEA are characterized by a high percentage of natural forest and wetland cover in urban and surrounding areas. However, due to the loose planning strategy, some ecologically important areas such as marshes or natural rainforests around the urban area in Vientiane have been gradually encroached upon. For example, the wetland in Fig. 9D was planned as a nature reserve, but was then replaced by paddy fields. Later, a part of this area was developed as a special economic zone with residential, entertainment, and service facilities in the past decade (Fig. 12) (Sharifi et al., 2014). The replacement of some ecologically important natural landscapes with urban land has inevitably led to negative consequences for the urban ecosystem, damaging the sustainable development capacity (Cobbinah et al., 2015; Nagendra et al., 2018). The encroachment of agricultural land by the urbanization process has caused suburban farmers to lose their farmland and disrupt their rural livelihoods, turning them into urban poor and bringing more social problems. Loss of original wetlands and natural forests can cause not only the destruction of habitats for a variety of species, but in turn reduce the ability of cities to regulate climate and hydrological conditions. How to effectively reconcile ecological conservation with socioeconomic development is a challenge in the urbanization process of SMCs. For Vientiane, Laos, which is experiencing a fast urbanization process, it is especially urgent to take in the experiences and lessons learned from other cities worldwide (Coenen et al., 2019). This can guide the orderly development of Vientiane itself and provide success stories for reference in the sustainable development of other SMCs in SEA.

5. Conclusion

The urban growth in Vientiane, Laos, represents the rapid urbanization process of small to medium-sized cities in Southeast Asia. This study proposed an effective method for accurate urban land mapping using a set of statistical indicators of time series optical and SAR images at finer resolution. The complementary optical and SAR time series statistical metrics showed great potential to improving the urban expansion monitoring for SMCs. The validation results show that the resultant urban land maps have high accuracy in terms of Kappa, overall, producer and user accuracy, and have higher accuracy than other products. However, the transferability of our method to other SMCs needs further exploration. The rapid urbanization process of Vientiane was characterized and analyzed based on resultant high-accuracy urban land datasets. Spatially, urban land densities in concentric rings decreased from the city center to the fringe, dropping quickly and then decreasing slowly. The pattern of the distance decay of urban land densities in Vientiane falls between the inverse S-shape and the two stages of linear decay. From 2000 to 2019, urban expansion in Vientiane was dominated by leapfrogging and edge-expansion growth.

Roadside development is another feature of Vientiane's urban expansion. Rapid urban sprawl poses a significant threat to the urban environment and sustainable development. Reconciling ecological conservation with urban development remains challenging in the urbanization process of Vientiane and other SMCs in SEA.

CRediT authorship contribution statement

Chong Huang: Conceptualization, Methodology, Software, Writing – original draft, Validation. **Chenchen Zhang:** Conceptualization, Writing – review & editing, Visualization, Validation.

Declaration of Competing Interest

The authors declare that they have no known competing financial interests or personal relationships that could have appeared to influence the work reported in this paper.

Acknowledgements

This research was funded by the CAS Earth Big Data Science Project, Grant No. XDA19060302; National Natural Science Foundation of China, Grant No. 42130508; National Key R&D Program of China, Grant No. 2018YFB0505403.

References

Belgiu, M., Drăguţ, L., 2016. Random forest in remote sensing: A review of applications and future directions. ISPRS J. Photogramm. Remote Sens. 114, 24–31.
Cao, H., Liu, J., Chen, J., Gao, J., Wang, G., Zhang, W., 2019. Spatiotemporal patterns of urban land use change in typical cities in the greater mekong subregion (GMS). Remote Sens. 11 (7), 801. https://doi.org/10.3390/rs11070801.
Chen, J., Chen, J., Liao, A., Cao, X., Chen, L., Chen, X., He, C., Han, G., Peng, S., Lu, M., Zhang, W., Tong, X., Mills, J., 2015. Global land cover mapping at 30 m resolution: A POK-based operational approach. ISPRS J. Photogramm. Remote Sens. 103, 7–27.
Cobbinah, P.B., Erdiaw-Kwasie, M.O., Amoateng, P., 2015. Africa's urbanisation: Implications for sustainable development. Cities 47, 62–72.
Coenen, L., Davidson, K., Gleeson, B., 2019. Situating C40 in the Evolution of Networked Urban Climate Governance. Global Policy 10 (4), 723–725.
Cohen, B., 2006. Urbanization in developing countries: Current trends, future projections, and key challenges for sustainability. Technol. Soc. 28 (1-2), 63–80.
Corbane, C., Politis, P., Syrris, V., Pesaresi, M., 2018. GHS built-up grid, derived from Sentinel-1 (2016), R2018A. European Commission, Joint Research Centre (JRC). Available online: http://data.europa.eu/89h/jrc-ghsl-10008 (accessed on 10 September 2018).
Deng, C., Zhu, Z., 2020. Continuous subpixel monitoring of urban impervious surface using Landsat time series. Remote Sens. Environ. 238, 110929. https://doi.org/10.1016/j.rse.2018.10.011.
Fei, W., Zhao, S., 2019. Urban land expansion in China's six megacities from 1978 to 2015. Sci. Total Environ. 664, 60–71.
Foody, G.M., 2002. Status of land cover classification accuracy assessment. Remote Sens. Environ. 80 (1), 185–201.
Gong, P., Li, X., Wang, J., Bai, Y., Chen, B., Hu, T., Liu, X., Xu, B., Yang, J., Zhang, W., Zhou, Y., 2020. Annual maps of global artificial impervious area (GAIA) between 1985 and 2018. Remote Sens. Environ. 236, 111510. https://doi.org/10.1016/j.rse.2019.111510.
Gong, P., Liu, H., Zhang, M., Li, C., Wang, J., Huang, H., Clinton, N., Ji, L., Li, W., Bai, Y., Chen, B., Xu, B., Zhu, Z., Yuan, C., Ping Suen, H., Guo, J., Xu, N., Li, W., Zhao, Y., Yang, J., Yu, C., Wang, X., Fu, H., Yu, L., Dronova, I., Hui, F., Cheng, X., Shi, X., Xiao, F., Liu, Q., Song, L., 2019. Stable classification with limited sample: transferring a 30-m resolution sample set collected in 2015 to mapping 10-m resolution global land cover in 2017. Sci. Bull. 64 (6), 370–373.
Guan, X., Huang, C., Liu, G., Meng, X., Liu, Q., 2015. Mapping rice cropping systems in Vietnam using an NDVI-based time-series similarity measurement based on DTW distance. Remote Sens. 8 (1), 19.
Hall, D., Hirsch, P., Li, T.M., 2011. Introduction to powers of exclusion: land dilemmas in Southeast Asia.
Herold, M., Liu, XiaoHang, Clarke, K.C., 2003. Spatial metrics and image texture for mapping urban land use. Photogramm. Eng. Remote Sens. 69 (9), 991–1001.
Henderson, F.M., Xia, Z.G., 1997. SAR applications in human settlement detection, population estimation and urban land use pattern analysis: a status report. IEEE Trans. Geosci. Remote Sens. 35 (1), 79–85.
Huang, C., Zhang, C., He, Y., Liu, Q., Li, H., Su, F., Liu, G., Bridhikitti, A., 2020. Land cover mapping in cloud-prone tropical areas using Sentinel-2 data: integrating spectral features with Ndvi temporal dynamics. Remote Sens. 12 (7), 1163. https://doi.org/10.3390/rs12071163.
Huete, A., Didan, K., Miura, T., Rodriguez, E.P., Gao, X., Ferreira, L.G., 2002. Overview of the radiometric and biophysical performance of the MODIS vegetation indices. Remote Sens. Environ. 83 (1–2), 195–213.
Huete, A., Liu, H., Batchily, K., Van Leeuwen, W.J., 1997. A comparison of vegetation indices over a global set of TM images for EOS-MODIS. Remote Sens. Environ. 59 (3), 440–451.
Jiao, L., 2015. Urban land density function: A new method to characterize urban expansion. Landscape Urban Plann. 139, 26–39.
Jongkroy, P., Thongbai, C., 2014. Patterns Of the Spatial Distribution of Urbanized Areas in Thailand. Kasetsart Journal of Social Sciences 35, 30–44.
Kuang, W., Chi, W., Lu, D., Dou, Y., 2014. A comparative analysis of megacity expansions in China and the US: Patterns, rates and driving forces. Landscape Urban Plann. 132, 121–135.
Leinenkugel, P., Esch, T., Kuenzer, C., 2011. Settlement detection and impervious surface estimation in the Mekong Delta using optical and SAR remote sensing data. Remote Sens. Environ. 115 (12), 3007–3019.
Lhermitte, S., Verbesselt, J., Verstraeten, W.W., Coppin, P., 2011. A comparison of time series similarity measures for classification and change detection of ecosystem dynamics. Remote Sens. Environ. 115 (12), 3129–3152.
Li, X., Zhou, Y., Zhu, Z., Liang, L., Yu, B., Cao, W., 2018. Mapping annual urban dynamics (1985–2015) using time series of Landsat data. Remote Sens. Environ. 216, 674–683.
Liaw, A., Wiener, M., 2002. Classification and regression by randomForest. R news 2, 18–22.
Lin, Y., Zhang, H., Lin, H., Gamba, P.E., Liu, X., 2020. Incorporating synthetic aperture radar and optical images to investigate the annual dynamics of anthropogenic impervious surface at large scale. Remote Sens. Environ. 242, 111757. https://doi.org/10.1016/j.rse.2020.111757.
Liu, C., Zhang, Q., Luo, H., Qi, S., Tao, S., Xu, H., Yao, Y., 2019. An efficient approach to capture continuous impervious surface dynamics using spatial-temporal rules and dense Landsat time series stacks. Remote Sens. Environ. 229, 114–132.
Liu, X., Hu, G., Chen, Y., Li, X., Xu, X., Li, S., Pei, F., Wang, S., 2018. High-resolution multi-temporal mapping of global urban land using Landsat images based on the Google Earth Engine Platform. Remote Sens. Environ. 209, 227–239.
Lu, D., Weng, Q., 2006. Use of impervious surface in urban land-use classification. Remote Sens. Environ. 102 (1-2), 146–160.
Martinez, W.L., Martinez, A.R., Solka, J.L., 2017. Exploratory data analysis with MATLAB®. Chapman and Hall/CRC.
Mauro, G., 2020. Rural-Urban Transition of Hanoi (Vietnam): Using Landsat Imagery to Map Its Recent Peri-Urbanization. ISPRS Int. J. Geo-Inf. 9 (11), 669. https://doi.org/10.3390/ijgi9110669.
Nagendra, H., Bai, X., Brondizio, E.S., Lwasa, S., 2018. The urban south and the predicament of global sustainability. Nat. Sustain. 1 (7), 341–349.
Nations, U., 2012. World Urbanization Prospects: The 2011 Revision. United Nations Department of Economic and Social Affairs/Population Division. UN Proceedings, New York.
Nations, U., 2019. World Urbanization Prospects: The 2018 Revision. United Nations Department of Economic and Social Affairs. Population Division, New York.
Niroula, G.S., Thapa, G.B., 2005. Impacts and causes of land fragmentation, and lessons learned from land consolidation in South Asia. Land use policy 22 (4), 358–372.
Petitjean, F., Inglada, J., Gancarski, P., 2012. Satellite image time series analysis under time warping. IEEE Trans. Geosci. Remote Sens. 50 (8), 3081–3095.
Qin, Y., Xiao, X., Dong, J., Chen, B., Liu, F., Zhang, G., Zhang, Y., Wang, J., Wu, X., 2017. Quantifying annual changes in built-up area in complex urban-rural landscapes from analyses of PALSAR and Landsat images. ISPRS J. Photogramm. Remote Sens. 124, 89–105.
Rahnama, M.R., Wyatt, R., Shaddel, L., 2020. A spatial-temporal analysis of urban growth in melbourne; Were local government areas moving toward compact or sprawl from 2001–2016? Appl. Geogr. 124, 102318. https://doi.org/10.1016/j.apgeog.2020.102318.
Reba, M., Seto, K.C., 2020. A systematic review and assessment of algorithms to detect, characterize, and monitor urban land change. Remote Sens. Environ. 242, 111739. https://doi.org/10.1016/j.rse.2020.111739.
Schneider, A., Friedl, M.A., Potere, D., 2010. Mapping global urban areas using MODIS 500-m data: New methods and datasets based on 'urban ecoregions'. Remote Sens. Environ. 114 (8), 1733–1746.
Schneider, A., Mertes, C.M., Tatem, A.J., Tan, B., Sulla-Menashe, D., Graves, S.J., Patel, N.N., Horton, J.A., Gaughan, A.E., Rollo, J.T., Schelly, I.H., Stevens, F.R., Dastur, A., 2015. A new urban landscape in East-Southeast Asia, 2000–2010. Environ. Res. Lett. 10 (3), 034002. https://doi.org/10.1088/1748-9326/10/3/034002.
Sexton, J.O., Song, X.-P., Huang, C., Channan, S., Baker, M.E., Townshend, J.R., 2013. Urban growth of the Washington, DC–Baltimore, MD metropolitan region from 1984 to 2010 by annual, Landsat-based estimates of impervious cover. Remote Sens. Environ. 129, 42–53.
Sharifi, A., Chiba, Y., Okamoto, K., Yokoyama, S., Murayama, A., 2014. Can master planning control and regulate urban growth in Vientiane, Laos? Landscape Urban Plann. 131, 1–13.
Shimada, M., Isoguchi, O., Tadono, T., Isono, K., 2009. PALSAR radiometric and geometric calibration. IEEE Trans. Geosci. Remote Sens. 47 (12), 3915–3932.
Sun, Z., Xu, R., Du, W., Wang, L., Lu, D., 2019. High-resolution urban land mapping in China from sentinel 1A/2 imagery based on Google Earth Engine. Remote Sens. 11 (7), 752. https://doi.org/10.3390/rs11070752.
Taubenböck, H., Esch, T., Felbier, A., Wiesner, M., Roth, A., Dech, S., 2012. Monitoring urbanization in mega cities from space. Remote Sens. Environ. 117, 162–176.
Torres, R., Snoeij, P., Geudtner, D., Bibby, D., Davidson, M., Attema, E., Potin, P., Rommen, B., Floury, N., Brown, M., Traver, I.N., Deghaye, P., Duesmann, B.,

Rosich, B., Miranda, N., Bruno, C., L'Abbate, M., Croci, R., Pietropaolo, A., Huchler, M., Rostan, F., 2012. GMES Sentinel-1 mission. Remote Sens. Environ. 120, 9–24.

Tucker, C.J., 1979. Red and photographic infrared linear combinations for monitoring vegetation. Remote Sens. Environ. 8 (2), 127–150.

Vongpraseuth, T., Choi, C.G., 2015. Globalization, foreign direct investment, and urban growth management: Policies and conflicts in Vientiane, Laos. Land Use Policy 42, 790–799.

Wang, B., Chen, Z., Zhu, A., Hao, Y., Xu, C., 2019. Multi-level classification based on trajectory features of time series for monitoring impervious surface expansions. Remote Sens. 11 (6), 640.

Wang, C., Wang, Y., Wang, R., Zheng, P., 2018. Modeling and evaluating land-use/land-cover change for urban planning and sustainability: a case study of Dongying city, China. J. Cleaner Prod. 172, 1529–1534.

Wang, Y., Li, M., 2019. Urban Impervious Surface Detection From Remote Sensing Images: A review of the methods and challenges[J]. IEEE Geosci. Remote Sens. Mag. 7 (3), 64–93.

WWIS, 2012. Weather information for Vientiane. Retrieved from: http:// worldweather. wmo.int/121/c00235.htm.

Xiao, X., Boles, S., Frolking, S., Li, C., Babu, J.Y., Salas, W., Moore, B., 2006. Mapping paddy rice agriculture in South and Southeast Asia using multi-temporal MODIS images. Remote Sens. Environ. 100 (1), 95–113.

Xiao, X., Hollinger, D., Aber, J., Goltz, M., Davidson, E.A., Zhang, Q., Moore, B., 2004. Satellite-based modeling of gross primary production in an evergreen needleleaf forest. Remote Sens. Environ. 89 (4), 519–534.

Xiao, X., Zhang, Q., Hollinger, D., Aber, J., Moore, B., 2005. Modeling gross primary production of an evergreen needleleaf forest using modis and climate data. Ecol. Appl. 15 (3), 954–969.

Xu, G., Dong, T., Cobbinah, P.B., Jiao, L., Sumari, N.S., Chai, B., Liu, Y., 2019a. Urban expansion and form changes across African cities with a global outlook: Spatiotemporal analysis of urban land densities. J. Cleaner Prod. 224, 802–810.

Xu, G., Jiao, L., Liu, J., Shi, Z., Zeng, C., Liu, Y., 2019b. Understanding urban expansion combining macro patterns and micro dynamics in three Southeast Asian megacities. Sci. Total Environ. 660, 375–383.

Zhang, H., Lin, H., Li, Y.u., Zhang, Y., Fang, C., 2016. Mapping urban impervious surface with dual-polarimetric SAR data: An improved method. Landscape Urban Plann. 151, 55–63.

Zhang, Y., Shen, W., Li, M., Lv, Y., 2020. Assessing spatio-temporal changes in forest cover and fragmentation under urban expansion in Nanjing, eastern China, from long-term Landsat observations (1987–2017). Appl. Geogr. 117, 102190. https://doi.org/10.1016/j.apgeog.2020.102190.

Zhao, S., Liu, S., Xu, C., Yuan, W., Sun, Y., Yan, W., Zhao, M., Henebry, G.M., Fang, J., 2018. Contemporary evolution and scaling of 32 major cities in China. Ecol. Appl. 28 (6), 1655–1668.

Zou, Z., Xiao, X., Dong, J., Qin, Y., Doughty, R.B., Menarguez, M.A., Zhang, G., Wang, J., 2018. Divergent trends of open-surface water body area in the contiguous United States from 1984 to 2016. Proc. Natl. Acad. Sci. U.S.A. 115 (15), 3810–3815.